Research paper

Monte Carlo uncertainty calculation of ^{210}Pb chronologies and accumulation rates of sediments and peat bogs

Joan-Albert Sanchez-Cabeza [a,*], Ana Carolina Ruiz-Fernández [b],
Jorge Feliciano Ontiveros-Cuadras [c], Libia Hascibe Pérez Bernal [b], Carolina Olid [d]

[a] Departamento de Procesos Oceánicos y Costeros, Instituto de Ciencias del Mar y Limnología, Universidad Nacional Autónoma de México, 04510 Ciudad de México, México
[b] Unidad Académica de Mazatlán, Instituto de Ciencias del Mar y Limnología, Universidad Nacional Autónoma de México, 82040 Mazatlán, México
[c] Posgrado en Ciencias del Mar y Limnología, Universidad Nacional Autónoma de México, Calz. Joel Montes Camarena s/n, 82040 Mazatlán, México
[d] Department of Ecology and Environmental Science, Umeå University, SE-901 87 Umeå, Sweden

ARTICLE INFO

ABSTRACT

^{210}Pb dating is a key technique to study sedimentary records of environmental change in the Anthropocene over a time scale of 100–150 years. Uncertainty estimation of ^{210}Pb ages and accumulation rates, when provided by the authors, are usually based on quadratic propagation of uncertainties. In this work, we describe the use of Monte Carlo simulation to estimate ^{210}Pb dating uncertainties in sediment and peat cores. The methodology allows, by using nowadays common computers, the assessment of ^{210}Pb dating uncertainties in a simple manner, using readily-accessible computers and widely-used proprietary spreadsheet software, and avoiding the derivation of rather complex formulae. Results were calculated and compared with quadratic propagation uncertainties in a marine, lacustrine and peat bog core. The analysis of the uncertainty budgets indicated that, overall, the total and unsupported (or base) ^{210}Pb concentrations are the largest contributors to uncertainty, as well as the layer depths when sediment accumulation rates were calculated. Beyond ^{210}Pb dating, the Monte Carlo scheme described here could be used in any field of the analytical sciences, including other radiochronological applications.

© 2014 Elsevier B.V. All rights reserved.

1. Introduction

Uncertainty assessment is essential to scientific research, irrespective of the complexity of the problem, the multiplicity of its sources and the methods used to derive it. It is common in natural sciences and has been described in numerous textbooks and guides (e.g. Taylor and Kuyatt, 1994; ISO, 1995; Ellison et al., 2000). For example, the Intergovernmental Panel on Climate Change (IPCC) devotes a half-page box to explain to decision-makers and society the treatment of uncertainty in their Synthesis of the 4th Assessment Report (IPCC, 2007). Indeed, uncertainty estimation should be a central matter in environmental studies (e.g. Refsgaard et al., 2007).

There are several ways to estimate uncertainty, and this largely depends on the problem addressed, the type and quality of data obtained and the researcher experience. Many methods have been

proposed and it is out of the scope of this work to revise them, but the reader will have no difficulty finding examples for his specific needs (for example, Refsgaard et al., 2007, lists 14 of them). One of the most widely used and accepted method is the quadratic propagation of uncertainties (QPU, see for example ISO, 1995). The combined uncertainty is assumed to follow a Gaussian distribution and is calculated as the quadratic sum of measurement uncertainties. Although this is not always the case, many experiments can be expected to follow a Gaussian (or very similar) distribution. In many cases, simple rules can be used to calculate QPU, but these only apply when variables are uncorrelated. Not only must researchers include all uncertainty sources of the experiment, but they must be also very careful to identify potential relations amongst variables (e.g. Taylor and Kuyatt, 1994). If variables are dependent, the covariance matrix amongst them must be obtained and used in the propagation. This makes analytical formulae complex, and calculation tedious and not easily implemented.

An important uncertainty estimation strategy is the use of Monte Carlo methods. In fact, Monte Carlo methods are commonly used to model processes themselves, but this is unnecessary if

analytical expressions exist, as it is common in radiochronology. Monte Carlo methods are based on the statistical concept that the repetition of an experiment many times allows one to obtain the frequency distribution of the results. Assuming that the final distribution is Gaussian, one may derive the mean value and its standard deviation, one of the most common ways to express uncertainty (ISO, 1995).

There are some examples of the use of Monte Carlo methods in radiochronology, including radiocarbon dating (e.g. Ramsey et al., 2001) and U–Th dating (e.g. Hellstrom, 2006). We only found one reference mentioning the use of Monte Carlo methods in relation to ^{210}Pb geochronology, a fundamental technique in Anthropocene studies (Binford, 1990). Although the number of laboratories using ^{210}Pb is not small, the lack of use of Monte Carlo methods might be due to the difficulty to develop specific computer programs to make the required simulations. In this work we propose the use of a widely-used spreadsheet to estimate ^{210}Pb dating Monte Carlo Uncertainties (MCU), as an alternative to QPU, when using the Constant Flux (CF) model (Sanchez-Cabeza and Ruiz-Fernández, 2012). The methodology was applied to two sediment cores and one peat core from different environments, length and time resolution, and results compared with common QPU expressions. This publication is accompanied by the Excel workbooks used to perform MCU analyses.

2. Monte Carlo methodology

The fundamentals, nomenclature and formulation of ^{210}Pb dating models (e.g. Krishnaswamy et al., 1971; Appleby and Oldfield, 1978; Robbins, 1978) were recently reviewed by Sanchez-Cabeza and Ruiz-Fernández (2012) and we closely followed their nomenclature and model formulation principles. In this work, we focused on the widely used Constant Flux model (CF, also known as Constant Rate of Supply — CRS) but the methodology can be extended to the other models and, indeed, other radiochronological methods.

As Microsoft Excel is the most widely used proprietary spreadsheet software, we used its nomenclature in this work. The reader is addressed to guides or books to get acquainted with its basic features. Other popular open software (LibreOffice, OpenOffice) could not be used because it does not allow the non-convergent iterative calculations used here. In this work, we used Microsoft Excel 2010, part of Microsoft Office Professional 2010 (32 bit version). The programme was run on a Sony Vaio VPCSB portable computer, with Intel Core i5-2450M CPU at 2.50 GHz and 4 GB RAM, provided with Microsoft Windows 7 Home Premium. Results relating to computing time should be referred to these hardware and software specifications. As computing power increases, it is likely that reported computing times are also reduced.

2.1. Spreadsheet setup

A little known feature of Excel is its capability to perform iterative analysis. When iterative calculations are entered, Excel prompts the user with the presence of a circular reference, as this is usually a user error. However, Monte Carlo is based on iterations that require the use of circular references in Excel. The scientist should first look for Options − Formulas and then activating Enable iterative calculation. During spreadsheet edition and preliminary calculations, we recommend selecting 1 in the box Maximum iterations (M). For the final Monte Carlo simulation, we recommend using a larger M such as 10,000, depending on the accuracy needed and the computer performance. Once this is done, every time anything is changed in the file the whole workbook is recalculated M times. As a simulation proceeds, the computer display is refreshed, making calculation slower, especially if graphics are

present. We recommend that, when the final simulation is run, a blank sheet is chosen for display before changing M. Any time the F9 key is pressed, the workbook is recalculated M times.

In order to simplify programming and readability, we defined constants and ranges by using the Names utility, which can be found within the Names Box that belongs to the main spreadsheet window. A summary of all magnitudes and names used is included in Table 1. Table 2 lists the Excel code used for calculation.

2.2. Switch and counter

We created separate spreadsheets to better illustrate the procedure described. The first spreadsheet was named Switch. Central to the uncertainty calculation by Monte Carlo methods is the addition of quadratic deviations from the true value, in order to calculate the standard deviation of the simulated magnitude (e.g. the model age). As the spreadsheet is iteratively recalculated, we needed to reset

Table 1
Magnitudes and names used in this work.

Magnitude	Excel name	Unit	Description
$A_a(i)$	Aa	Bq	Accumulated deposit above a layer
$A_b(i)$	Ab	Bq	Accumulated deposit below a layer
$T(i)$	Agel	A.D.	Calendar age of a layer
T_i	Ages	A.D.	Calendar age of a section
—	Code	—	Sample code
—	Counter	—	Number of iterations performed
C_i	Cs	Bq kg^{-1}	Concentration in a section
C_1	Conc1	—	Concentration of variable 1
φ	D	cm	Internal core diameter
$\rho(i)$	Del	g cm^{-3}	Dry bulk density of a layer
ρ_i	Des	g cm^{-3}	Dry bulk density of a section
ΔA_i	Dep	Bq	Total deposit in a section
Δt	Dt	a	Formation period of a section
Δz	Dz	cm	Width of a section
f	Flux	Bq m^{-2} a^{-1}	Flux to the core surface
F_1	Flux1	—	Flux of variable 1
I	I	Bq	Core inventory
λ	L	a^{-1}	^{210}Pb decay constant
—	lnCs	—	Natural logarithm of a section concentration
$r(i)$	MARl	kg m^{-2} a^{-1}	Mass accumulation rate of a layer
r_i	MARs	kg m^{-2} a^{-1}	Mass accumulation rate of a section
Δm_i	M	g	Dry mass of a section
$\Sigma \Delta m(i)$	SMl	g	Layer accumulated mass
$\Sigma \Delta m_i$	SMs	g	Section accumulated mass
$m(i)$	Ml	g cm^{-2}	Layer mass depth
m_i	Ms	g cm^{-2}	Section mass depth
^{210}Pb	Pb210	Bq kg^{-1}	Total ^{210}Pb concentration
^{226}Ra	Ra226	Bq kg^{-1}	^{226}Ra concentration
—	Red	—	Uncertainty reduction factor
S	S	cm^{-2}	Core cross section
$s(i)$	SARl	cm a^{-1}	Sediment accumulation rate of a layer
s_i	SARs	cm a^{-1}	Sediment accumulation rate of a section
—	Switch	—	Field used to reset sqMagnitude
$T_{1/2}$	T	a	^{210}Pb radioactive half-life
$T(0)$	T0	a	Sampling date
$t(i)$	Tl	a	Time elapsed since a layer formation
t_i	Ts	a	Mean time of a section
$z(i)$	Zl	cm	Depth of a layer
z_i	Zs	cm	Mean depth of a section
Derived magnitudes			
—	uMagnitude		Uncertainty of measured magnitude
—	rMagnitude		Generated random number of a magnitude
—	sqMagnitude		Sum of squares of deviations of a magnitude
—	urMagnitude		Monte Carlo uncertainty (MCU) of a magnitude

Table 2
Excel code used for calculations.

Code line	Function	Calculation/Description	Comment
Switch Sheet			
1	Switch	Manually: 0 (delete), 1 (start)	Used to restart all iterative calculations.
2	Counter	IF(Switch = 0,0,Counter + 1)	Counts the number of iterations performed.
Constants sheet			
3	D	Diameter (cm)	Measurement.
4	uD	D uncertainty (cm)	Provided by scientist.
5	rD	rD − rD + NORMINV(RAND(),D,uD/Red)	Monte Carlo (MC) simulated value of diameter.
6	S	PI()*(D/2)^2	Corer surface section.
7	sqS	IF(Switch = 0,0,sqS + (rS − S)^2)	Sum of squares of deviations of the simulated surface.
8	urS	SQRT(sqS/Counter)*Red	MCU of the surface.
9	T	^{210}Pb half-life (a)	Published value.
10	uT	T uncertainty (a)	Published value. 1 sigma value must be used.
11	rT	rT − rT + NORMINV(RAND(),T,uT/Red)	Simulated ^{210}Pb half-life.
12	L	LN(2)/T	Decay constant (lambda)
13	rL	LN(2)/rT	Simulated decay constant.
14	sqL	IF(Switch = 0,0,sqL + (rL − L)^2)	Sum of squares of deviations of the simulated decay constant.
15	urL	SQRT(sqL/Counter)*Red	MCU of the decay constant.
Depth-mass sheet			
16	Code	Sample code	Provided by scientist.
17	Zl	Measured layer depth (cm)	Provided by scientist.
18	uZl	Zl uncertainty (cm)	Provided by scientist.
19	rZl	rZl − rZl + NORMINV(RAND(),Zl,uZl/Red)	Simulated layer depth.
20	Zs	AVERAGE(Zl(i − 1), Zl(i))	Section depth.
21	rZs	AVERAGE(rZl(i − 1),rZl(i))	Simulated section depth.
22	sqZs	IF(Switch = 0,0,sqZs + (rZs − Zs)^2)	Sum of squares of deviations of the simulated section depth.
23	urZs	SQRT(sqZs/Counter)*Red	MCU of the section depth.
24	Dz	Zl(i) − Zl(i − 1)	Section width.
25	rDz	rZl(i) − rZl(i − 1)	Simulated section width.
26	sqDz	IF(Switch = 0,0,sqDz + (rDz − Dz)^2)	Sum of squares of deviations of the simulated section width.
27	urDz	SQRT(sqDz/Counter)*Red	MCU of the section width.
28	M	Measured section mass (g)	Provided by scientist.
29	uM	M uncertainty (g)	Provided by scientist.
30	rM	rM − rM + NORMINV(RAND(),M,uM/Red)	Simulated section mass.
31	SMl(0)	0	Layer accumulated mass of top layer.
32	uSMl(0)	0	Uncertainty of the layer accumulated mass of top layer.
33	SMl	SMl(i − 1) + M	Layer accumulated mass.
34	rSMl	rSMl(i − 1) + rM	Simulated layer accumulated mass.
35	sqSMl	IF(Switch = 0,0,sqSMl + (rSMl − SMl)^2)	Sum of squares of deviations of the simulated layer accumulated mass.
36	urSMl	SQRT(sqSMl/Counter)*Red	MCU of the layer accumulated mass.
37	Ml	SMl/S	Layer mass depth.
38	rMl	rSMl/rS	Simulated layer mass depth.
39	sqMl	IF(Switch = =0,0,sqMl + (rMl − Ml)^2)	Sum of squares of deviations of the simulated layer mass depth.
40	urMl	SQRT(sqMl/Counter)*Red	MCU of the layer mass depth.
41	SMs	SMs(i − 1) + M/2	Section accumulated mass.
42	rSMs	rSMs(i − 1) + rM/2	Simulated section accumulated mass.
43	sqSMs	IF(Switch = 0,0,sqSMs + (rSMs − SMs)^2)	Sum of squares of deviations of the simulated section accumulated mass.
44	urSMs	SQRT(sqSMs/Counter)*Red	MCU of the section accumulated mass.
45	Ms	SMs/S	Section mass depth.
46	rMs	rSMs/rS	Simulated section mass depth.
47	sqMs	IF(Switch = 0,0,sqMs + (rMs − Ms)^2)	Sum of squares of deviations of the simulated section mass depth.
48	urMs	SQRT(sqMs/Counter)*Red	MCU of the section mass depth.
49	Des	M/S/Dz	Dry bulk density of a section.
50	rDes	rM/rS/rDz	Simulated dry bulk density of a section.
51	sqDes	IF(Switch = 0,0,sqDes + (rDes − Des)^2)	Sum of squares of deviations of the simulated dry bulk density of a section.
52	urDes	SQRT(sqDes/Counter)*Red	MCU of the dry bulk density of a section.
53	Del	AVERAGE(Des(i − 1), Des(i))	Dry bulk density of a layer.
54	rDel	AVERAGE(rDes(i − 1),rDes(i))	Simulated dry bulk density of a layer.
55	sqDel	IF(Switch = 0,0,sqDel + (rDel − Del)^2)	Sum of squares of deviations of the simulated dry bulk density of a layer.
56	urDel	SQRT(sqDel/Counter)*Red	MCU of the dry bulk density of a layer.
Concentrations sheet			
57	Pb210	Measured ^{210}Pb concentration (Bq kg^{-1})	Provided by analyst.
58	uPb210	Pb210 concentration uncertainty	Provided by analyst.
59	rPb210	rPb210-rPb210 + NORMINV(RAND(),Pb210,uPb210/Red)	Simulated total ^{210}Pb concentration.
60	Ra226	Measured ^{226}Ra concentration (Bq kg^{-1})	Provided by analyst.
61	uRa226	Ra226 concentration uncertainty	Provided by analyst.
62	rRa226	rRa226-rRa226 + NORMINV(RAND(),Ra226,uRa226/Red)	Simulated ^{226}Ra concentration.
63	Cs	Pb210-Ra226	Excess ^{210}Pb.
64	rCs	rPb210-rRa226	Simulated excess ^{210}Pb.

Table 2 (continued)

Code line	Function	Calculation/Description	Comment
65	sqCs	IF(Switch = 0,0,sqCs + (rCs − Cs)^2)	Sum of squares of deviations of the simulated excess [210]Pb.
66	urCs	SQRT(sqCs/Counter)*Red	MCU of the excess [210]Pb.
67	Dep	Cs*M/1000	Total deposit in a section.
68	rDep	rCs*rM/1000	Simulated total deposit in a section.
69	sqDep	IF(Switch = 0,0,sqDep + (rDep − Dep)^2)	Sum of squares of deviations of the simulated total deposit in a section.
70	urDep	SQRT(sqDep/Counter)*Red	MCU of the total deposit in a section.
CF sheet			
71	Ab	Ab(i + 1) + Dep(i + 1)	Accumulated deposit below a layer.
72	rAb	rAb(i + 1) + rDep(i + 1)	Simulated accumulated deposit below a layer.
73	sqAb	IF(Switch = 0,0,sqAb + (rAb − Ab)^2)	Sum of squares of deviations of the simulated accumulated deposit below a layer.
74	urAb	SQRT(sqAb/Counter)*Red	MCU of the accumulated deposit below a layer.
75	Aa(0)	0	Accumulated deposit above layer 0.
76	uAa(0)	0	Uncertainty of the accumulated deposit above layer 0.
77	Aa	Aa(i − 1) + Dep	Accumulated deposit above a layer.
78	rAa	rAa(i − 1) + rDep	Simulated accumulated deposit above a layer.
79	sqAa	IF(Switch = 0,0,sqAa + (rAa − Aa)^2)	Sum of squares of deviations of the simulated accumulated deposit above a layer.
80	urAa	SQRT(sqAa/Counter)*Red	MCU of the accumulated deposit above a layer.
81	Flux	L*I/S*10000	[210]Pb flux to the core surface.
82	rF	rL*rI/rS*10000	Simulated ^{210}Pb flux to the core surface.
83	sqF	IF(Switch = 0,0,sqF + (rF − Flux)^2)	Sum of squares of deviations of the simulated ^{210}Pb flux to the core surface.
84	urF	SQRT(sqF/Counter)*Red	MCU of the ^{210}Pb flux to the core surface.
85	Tl	LN(1 + Aa/Ab)/L	Layer age.
86	rTl	LN(1 + rAa/rAb)/rL	Simulated layer age.
87	sqTl	IF(Switch = 0,0,sqTl + (rTl − Tl)^2)	Sum of squares of deviations of the simulated layer age.
88	urTl	SQRT(sqTl/Counter)*Red	MCU of the layer age.
89	Agel	T0−Tl	Layer calendar age.
90	Ages	AVERAGE(Agel(i − 1),Agel(i))	Section calendar age.
91	Dt	Tl(i) − Tl(i − 1)	Formation period of a section.
92	rDt	rTl(i) − rTl(i − 1)	Simulated formation period of a section.
93	sqDt	IF(Switch = 0,0,sqDt + (rDt − Dt)^2)	Sum of squares of deviations of the simulated formation period of a section.
94	urDt	SQRT(sqDt/Counter)*Red	MCU of the formation period of a section.
95	MARs	L/S*(Ab/Cs*1000 + M/2)	Mass accumulation rate of a section.
96	rMARs	rL/rS*(rAb/rCs*1000 + rM/2)	Simulated mass accumulation rate of a section.
97	sqMARs	IF(Switch = 0,0,sqMARs + (rMARs − MARs)^2)	Sum of squares of deviations of the simulated mass accumulation rate of a section.
98	urMARs	SQRT(sqMARs/Counter)*Red	MCU of the mass accumulation rate of a section.
99	SARs	MARs/Des	Sediment accumulation rate of a section.
100	rSARs	rMARs/rDes	Simulated sediment accumulation rate of a section.
101	sqSARs	IF(Switch = 0,0,sqSARs + (rSARs − SARs)^2)	Sum of squares of deviations of the simulated sediment accumulation rate of a section.
102	urSARs	SQRT(sqSARs/Counter)*Red	MCU of the sediment accumulation rate of a section.
103	Conc1	Concentration of variable 1	Provided by analyst.
104	uConc1	Uncertainty of variable 1	Provided by analyst.
105	rConc1	rConc1 − rConc1 + INV.NORM(ALEATORIO(),Conc1, uConc1/Red)	Simulated concentration of variable 1.
106	Flux1	MARs*Conc1	Flux of variable 1.
107	rFlux1	rMARs*rConc1	Simulated flux of variable 1.
108	sqFlux1	IF(Switch = 0,0,sqFlux1 + (Flux1 − rFlux1)^2)	Sum of squares of deviations of the simulated flux of variable 1.
109	urFlux1	SQRT(sqFlux1/Counter)*Red	MCU of the flux of variable 1.

cells where the additions are accumulated. To do this, we defined a *Switch* (Table 2, line 1) that controls the start of each simulation. It can have a value of zero, when the relevant cells are set to zero, or any other value (e.g. 1) when simulation takes place.

In order to calculate standard deviations and to know the number of simulations performed, we used a *Counter* (Table 2, line 2). The *Counter* is reset when the *Switch* is zero, and it is increased by 1 after each simulation (for example, when pressing the key F9). It is useful to make all A1 cells in other sheets equal to *Counter*, so we see the iteration number in each sheet.

2.3. Random value generation

In Monte Carlo calculations one needs to generate a random number for a simulated magnitude following a suitable probability distribution function (PDF). Excel provides the random generation function named RAND(), which provides a random number between 0 and 1. In our work, we assumed that all parameters followed a Gaussian PDF (type A uncertainty, Taylor and Kuyatt, 1994), although other PDFs could also be implemented. In order to obtain a random number following this distribution, we used the Excel function NORMINV(RAND(), mean, sigma), where mean and sigma are the value and standard deviation of the measured quantity.

A simple example is the case of the ^{210}Pb decay constant (λ, named L in the sheet *Constants*), which is used here to illustrate the basic principles of the Monte Carlo Uncertainty (MCU) method described. The usually tabulated value is the half-life $T_{1/2} = 22.23 \pm 0.12\ a$ (DDEP, 2012) and lambda is calculated as:

$$\lambda = \frac{\ln(2)}{T_{1/2}} = 0.03118\ a^{-1}$$

Following the QPU rules, the uncertainty is:

$$u(\lambda) = \lambda \frac{u(T_{1/2})}{T_{1/2}} = 0.00017 \, a^{-1}$$

This uncertainty is of the order of 0.5% and, though small, was taken into consideration in calculating the age uncertainty. First, we generated a random value for $T_{1/2}$ (rT) by using the expression:

$$rT = NORMINV(RAND(), T, uT)$$

where T and uT are the Excel names assigned to the cells containing the $T_{1/2}$ value and its uncertainty. For each iteration the value or rT changes. In order to ensure that this occurs when multiple iterations are run, it was found convenient to force calculation by causing a circular reference as follows:

$$rT = rT - rT + NORMINV(RAND(), T, uT)$$

2.4. Monte Carlo uncertainty calculation

Random values were generated for measured magnitudes (thus with known uncertainties) and these were used to calculate the uncertainties of the derived parameters. In the case of *Lambda* (L), its random value rL can be calculated with the rT value (Table 2, line 13). Although unlikely in this case, due to the small uncertainty of $T_{1/2}$, a random number can be close to zero, which would cause a calculation overflow and an error would be displayed in this (and any related) cells. This was a common problem when, for example, computing accumulation rates. In order to reduce the probability of obtaining random values close to zero, we adopted an *uncertainty reduction* approach by dividing the measured uncertainty by a constant ($k = $ Red), which we set arbitrarily equal to 100. Other values were tried, but the same results were obtained once a sufficiently large value was used. In general, the QPU of a generic function with independent variables can be calculated as:

$$u(f) = \sqrt{\sum_i \left(\frac{\partial f}{\partial x_i}\right)^2 u^2(x_i)}$$

When the uncertainty is reduced by a factor k, the new uncertainty is:

$$u'(f) = \sqrt{\sum_i \left(\frac{\partial f}{\partial x_i}\right)^2 \left(\frac{u(x_i)}{k}\right)^2} = \frac{u(f)}{k}$$

so the real uncertainty can be calculated by multiplying the calculation result by k. Therefore, the random value of the half-life is, finally:

$$rT = rT - rT + NORMINV(RAND(), T, uT/Red)$$

The uncertainty of a magnitude x (with random value x_i and true value $\bar{x}$) that follows a Gaussian distribution is its standard deviation σ, which for a large number of iteration can be written as:

$$\sigma = \sqrt{\frac{\sum_{i=1}^n (x_i - \bar{x})^2}{n}}$$

For each iteration, we added the quadratic deviation $(x - \bar{x})^2$ to the contents of the calculation cell (named sqL) and then the MCU was caculated (urL; Table 2, lines 13—14). In this simple case, the MCU converged to the QPU within 1% in less than 1000 iterations (Fig. 1), which took less than 2 s of computing time.
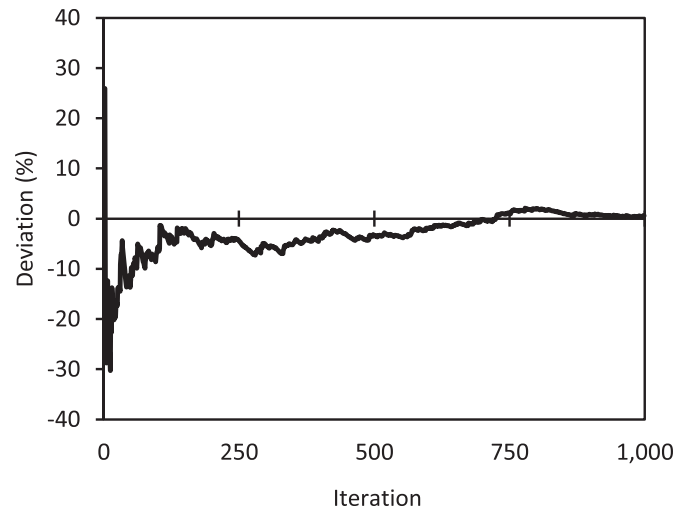

Fig. 1. Convergence (percent deviation) of MCU to QPU for Lambda.

2.5. Dependent variables

Simple QPU (i.e. without the calculation of the covariance matrix) can only be used in the case of independent variables. In the case of dependent variables, the use of the simple rules commonly used for additions, subtractions, products and divisions (e.g. Taylor and Kuyatt, 1994) can easily lead to mistakes. For example, the sediment core surface, used in ^{210}Pb dating to compute the excess (or unsupported) ^{210}Pb (^{210}Pb$_{ex}$) flux and activities per unit surface, can be calculated as

$$S = \pi \left(\frac{\phi}{2}\right)^2 = \frac{\pi}{4}\phi^2$$

where ϕ is the inner core diameter (for example, $\phi = 10.0$ cm, measured with a ruler of 0.1 cm precision P; $S = 78.5$ cm^2). In this case, the uncertainty $u(\phi)$ is Type B (Taylor and Kuyatt, 1994), and the uncertainty corresponding to a rectangular distribution is:

$$u(\phi) = \frac{P}{\sqrt{3}}$$

namely 0.06 cm. If the expression used to calculate the surface S is treated as a constant multiplied by the product $\phi*\phi$, the wrong QPU expression would be $u(S) = (\pi/2\sqrt{2})\phi \, u(\phi)$. However, by using the QPU general expression the correct expression for the surface uncertainty is:

$$u(S) = \frac{\pi}{2}\phi \, u(\phi)$$

yielding $u(S) = 0.9$ cm^2, which is $\sqrt{2} = 1.4$ times larger than the wrongly calculated one. The calculation of urS is shown in Table 2 (lines 5—8) and also yields 0.9 cm^2, which confirms the need to use independent variables when calculating QPU.

3. Dating of TEHUA II

The sediment core TEHUA II was collected from the Tehuantepec Gulf (Mexico) and is fully described by Ruiz-Fernández et al. (2009). Briefly, the 18 cm core was collected with a Reineck-type corer during the TEHUA II oceanographic cruise in October 2004 and data were provided for 1 cm intervals (Sanchez-Cabeza and Ruiz-Fernández, 2012). The dating and uncertainty calculations were

organized in sequential spreadsheets of the workbook "TEHUA II MCU.XLS" (Supplementary Information). Only details relevant to this work are discussed here and the reader is referred to that publication for further details.

We used the subscript i to name the magnitudes measured in each section. For example, the excess ^{210}Pb (^{210}Pb$_{ex}$) in the surficial section is named as C_1, and so forth. In the Constant Flux (CF) model, equations refer to quantities in infinitesimal layers that are derived from calculation. We used (i) to refer to the consecutive number of the surface cut (layer) when sampling. For example, (0) refers to the core surface (Layer 0) and (1) to the first surface cut below the surface (usually of the order of 1 cm). Therefore, section 1 is contained between layers (0) and (1) and, in the columns referring to sections, the row Layer 0 is empty. For example, Δm_i for sample TEH 4−5 is the mass of section 4−5 cm, and $m(i)$ in the same row is the lower layer mass depth (5 cm) of that section. When layer values are calculated (such as in CF dating), section values were obtained by averaging the upper and lower layer values.

3.1. Depth and mass

The principals of MCU calculation for masses and derived variables are similar to those described above, i.e. identification of magnitudes with measured uncertainties, Monte Carlo simulation of the Gaussian distributions, calculation of derived quantities with the simulated values and iterative calculation of the standard deviation of the new distributions.

In order to facilitate the use of the spreadsheet, we denoted each magnitude followed by {…}l in case of layers, and {…}s in case of sections. There were two measured uncertainty sources in this spreadsheet. The layer depth ($z(i)$, Zl) was the only depth measurement performed in the experiment and has important implications for the calculation of other quantities such as the section dry bulk density. The uncertainty of the layer depth ($u(z(i))$, uZl) is a type B uncertainty and was assumed to follow a rectangular probability distribution. As the measurement precision was 0.1 cm, $u(z(i)) = 0.1/\sqrt{3} = 0.06$ cm. The simulation of the layer depth is shown in Table 2 (line 19). The other uncertainty source is the measured the section mass (Δm_i, M), with a type B uncertainty ($u(\Delta m_i)$, uM = 0.001 g in this case), which was similarly simulated (Table 2, line 30).

As a section is defined by two consecutive layers, the mean section depth (z_i, Zs) uncertainty ($u(z_i)$, urZs) must take into account the uncertainties of the upper and lower layers. In this case, we could not summarize the calculation using a single Excel expression because it refers to two cells in the same column (Table 2, lines 20−23). Needless to say, MCU and QPU are identical after enough (over 1000) simulations were performed. A relevant magnitude is the section depth (Δz_i, DZ), used to calculate densities (Table 2, lines 24−27).

3.2. Mass depth

Most ^{210}Pb dating models require the use of the layer mass depth (i.e. the accumulated mass per unit surface: $m(i)$, Ml; Table 2, lines 37−40) instead of the linear depth ($z(i)$) to overcome the problems of compaction. It is also recommended to interpret sedimentary records, such as climate proxies and pollutant concentrations, as a function of section mass depth (m_i, Ms, Table 2, lines 45−48). To calculate them it was convenient to calculate the layer accumulated mass ($\Sigma\Delta m(i)$, SMl; Table 2, lines 33−36). Similar expressions were used for the section accumulated mass (SMs; Table 2, lines 41−44). Finally, density uncertainties depend on the mass, surface and section width uncertainties. The calculation of

section densities ($\rho_i = \Delta m_i/(S \cdot \Delta z_i)$, Des) and its MCU are shown in Table 2 (lines 49−52). Similar expressions were used for the layer density ($\rho(i)$, Table 2, lines 53−56). In both cases, MCU and QPU uncertainties were identical.

3.3. Concentrations

^{210}Pb concentrations (Pb210) are experimentally determined and their uncertainties (uPb210) should be provided by the analytical laboratory (Table 2, lines 57−58). We note that the methodology described here can be made extensive to uncertainty calculation of any process, as for example the analysis of ^{210}Pb itself. The Monte Carlo simulation expression is shown in Table 2 (line 59). As described by Sanchez-Cabeza and Ruiz-Fernández (2012), based on work by Binford (1990), ^{226}Ra (Ra226) in this core was calculated from the average of the almost constant ^{210}Pb activities recorded in the last 3 core sections, assumed to be in equilibrium with ^{226}Ra. Its uncertainty (uRa226) was estimated as the standard deviation of these values and the Monte Carlo simulated value was calculated (Table 2, lines 60−62).

The magnitude used for dating is ^{210}Pb$_{ex}$ (Cs), which was calculated as:

$$C_i = {}^{210}\text{Pb} - {}^{226}\text{Ra}$$

(Table 2, lines 63−66). Because at the profile base ^{210}Pb and ^{226}Ra are very close, it is not uncommon to find low values with large uncertainties (e.g. $C_{15} = 4.8 \pm 1.9$ Bq kg^{-1}), so the random number generator RAND() can provide negative and also close to zero values. This was solved with the previously described uncertainty reduction approach of this work. As the uncertainty sources have increased, convergence is now observed after about 3000−4000 iterations (Fig. 2). At this stage, the computing time of 1000 iterations, when run from a blank sheet, was still less than 1 s. When the iterations were increased to 10,000 the computing time was close to 5 s.

The deposit (ΔA_i, Dep), i.e. the total activity of the section (in Bq) is:

$$\Delta A_i = C_i \, \Delta m_i$$

which was calculated as shown in Table 2 (lines 67−70), where the factor 1000 takes into account the appropriate units conversion.

3.4. CF model

Once all basic magnitudes were calculated, we dated the core by using the CF model. In order to make MCU comparable to QPU, we derived expressions with independent variables. To do this, we followed the scheme proposed by Appleby (2001) by computing the total deposition above and below, respectively, a certain layer j:

$$A_a(i) = \sum_{j=0}^{j=i} \Delta A_j \quad A_b(i) = \sum_{j=i+1}^{j=\infty} \Delta A_j$$

Calculation is shown in Table 2 (lines 71−80). The total core inventory I is then equal to $A_b(0)$.

A relevant variable in ^{210}Pb radiochronology is the ^{210}Pb$_{ex}$ flux to the core surface (f, Flux), which is assumed to be constant and is:

$$f = \lambda I$$

which was calculated as shown in Table 2 (lines 81−84). In the case of TEHUA II the flux was 303 ± 8 Bq m^{-2} a^{-1}, significantly larger those observed in coastal sediments (Ruiz-Fernández et al., 2009)
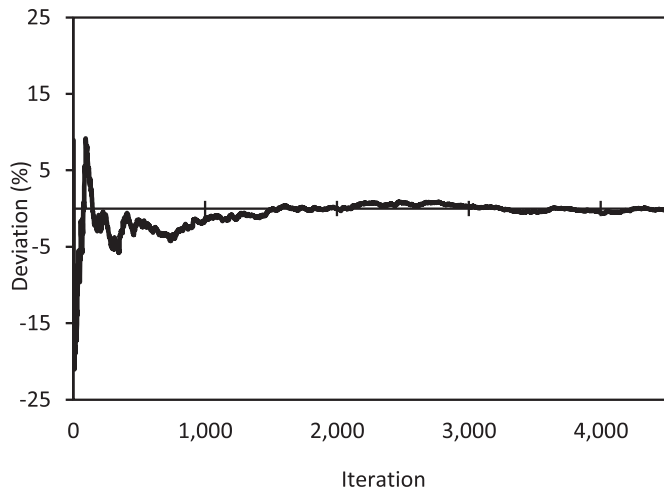
Fig. 2. Convergence (percent deviation) of MCU to QPU for $^{210}Pb_{ex}$ in one section (C_i of TEHUA II section 7–8).

and thus showing the *in situ* production and scavenging of ^{210}Pb from the water column.

The CF layer age was calculated with the expression:

$$t(i) = \frac{1}{\lambda} \ln\left(1 + \frac{A_a(i)}{A_b(i)}\right)$$

The variables of this expression are independent so one may be tempted to use a simple QPU expression such as:

$$u(t(i)) = t(i)\sqrt{\left(\frac{u(\lambda)}{\lambda}\right)^2 + \left(\frac{u(A_a(i))}{A_a(i)}\right)^2 + \left(\frac{u(A_b(i))}{A_b(i)}\right)^2}$$

However, this is incorrect for expressions including a logarithm. The use of the quadratic propagation formula yields:

$$u(t(i)) = \frac{1}{\lambda}\sqrt{(t(i)u(\lambda))^2 + \left(\frac{u(A_a(i))}{I}\right)^2 + \left(\frac{A_a(i)u(A_b(i))}{A_b(i)I}\right)^2}$$

The MCU Excel expressions are much more simple and do not require algebraic manipulations (Table 2, lines 85–88). In the case of TEHUA II, although the difference of the correct to the wrong expressions was only 6% in the top layer, this difference was close to −400%, i.e. 4-fold smaller, in the bottom section (Fig. 3). The important improvement reached with MCU allowed, in this case, to
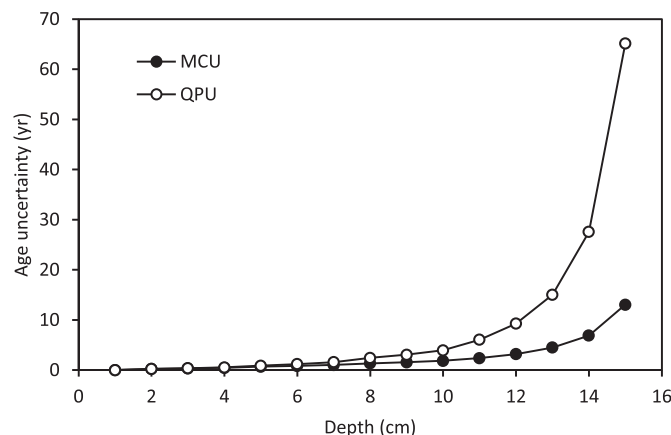
extend the use of the ^{210}Pb dating methodology beyond 150 a with a lower than 10% age uncertainty (Table 3). This is a surprising result which cannot be generalized as the age uncertainty depends on many variables. The layer (Agel) and section (Ages) ages were then easily calculated (Table 2, lines 89–90).

The CF model provides ages for the core layers, i.e. the upper and lower boundaries of each section. Although one may compute the mean section age, useful for the interpretation of the time trends of change proxies and pollution indicators, the radiochronologist should be careful to indicate the section age range, to which interpretation must be related (see for example Sanchez-Cabeza et al., 2012). In this sense, the ^{210}Pb age uncertainty becomes critical when attributing causes in environmental reconstruction studies. In the case of the TEHUA II core, layer ages and MCU uncertainties ranged from 3.6 ± 0.2 to 159 ± 13 a (Table 3).

We compared the MCU methodology with uncertainty results reported for Lake Windermere (Appleby, 2001). The conclusions of this comparison must be used with caution, as not all needed information (such as individual section masses) were reported and we derived them by calculation, and some deviations may be caused by numerical rounding of the reported values. The MCU age uncertainties ranged from 0.05 a (section 0–1 cm) to 12 a (section 24–25 cm), identical to the uncertainties reported for the core bottom, but rapidly decreased towards the core surface, were they were found to be 20 times lower.

3.5. Accumulation rates

As outlined by Sanchez-Cabeza and Ruiz-Fernández (2012), sediment accumulation can be quantified through the sediment accumulation rate (SAR, cm a^{-1}) and the mass accumulation rate (MAR, g cm^{-2} a^{-1}). Although SAR is a more intuitive quantity, as it has speed units, it is affected by compaction, which is not the case for MAR. Furthermore, MAR is extremely useful to convert concentrations (e.g. mg kg^{-1} of a contaminant) to fluxes, of much value in environmental studies (for example pollutants: mg cm^{-2} a^{-1}).

The simplest (and most common) way to estimate mass accumulation rate is through the simple expression:

$$r_i = \frac{\Delta m_i}{S\Delta t_i}$$

where Δt_i values are calculated following Table 2 (lines 91–94). QPU in this case yielded uncertainties ranging from 6 to 217% (top and bottom sections, respectively). These uncertainties, too large

Table 3
CF (Constant Flux) ages and Monte Carlo derived uncertainties in core TEHUA II (Gulf of Tehuantepec, Mexico).

Layer (cm)	CF age (a)	Calendar age (A.D.)	Age uncertainty (a)	Section (cm)	Mean calendar age (a)
0	0.0	2004.8	0.0	0–1	2003.0
1	3.6	2001.2	0.2	1–2	1999.4
2	7.1	1997.7	0.3	2–3	1995.5
3	11.4	1993.4	0.4	3–4	1989.3
4	19.5	1985.3	0.7	4–5	1982.0
5	26.0	1978.8	0.8	5–6	1975.5
6	32.6	1972.2	1.0	6–7	1965.9
7	45.1	1959.7	1.3	7–8	1956.5
8	51.4	1953.4	1.6	8–9	1949.7
9	58.8	1946.0	1.8	9–10	1938.0
10	75	1930	2	10–11	1923
11	89	1916	3	11–12	1908
12	105	1900	4	12–13	1889
13	127	1878	7	13–14	1863
14	159	1845	13		

Fig. 3. Comparison of ages QPU and MCU in core TEHUA II.

for many applications and unacceptably large in the bottom sections, were clearly affected by the non-independence of the ages (and thus Δt).

A better strategy is to use the CF MAR expression:

$$r(i) = \frac{\lambda A_b(i)}{C(i)}$$

When transforming the expression to calculate the MAR of a section, a careful examination revealed that the concentration of section i (C_i) appears in both terms of the fraction. The expression with independent variables is:

$$r = \frac{\lambda}{S}\left(\frac{1000A_b}{C_i} + \frac{\Delta m_i}{2}\right)$$

where the factor 1000 reflects unit changes (g to kg). Calculation is shown in Table 2 (lines 95–98). MARs ranged from 0.297 ± 0.019 to 0.049 ± 0.012 g cm^{-2} a^{-1} (Fig. 4) so uncertainties ranged from 6 to 25% of MAR. This represents an improvement from the previous calculation which ranged from 6% in the top to 689% in the bottom sections. Thus, the uncertainty values obtained with this scheme make MAR more scientifically meaningful along the core. When comparing the MCU methodology with results reported for Lake Windermere (Appleby, 2001), the MCU MAR uncertainties ranged from 0.04 to 0.09 g cm^{-2} a^{-1}, similar but in average 11% lower than those reported.

The sediment accumulation rate (SAR) is much used by radiochronologists because it is more intuitive and needed when the relative height of a certain section is of scientific value, such as when knowing the rate of accretion is important, such as in the study of sea level change (Lynch et al., 1989), or when the risk of silting up is real (e.g. in ports and lagoons). Again, a simple approach would be to directly calculate SAR as

$$s_i = \frac{\Delta z_i}{\Delta t_i}$$

which yields high uncertainties, ranging from 9 to 218%. SAR can also be easily calculated from CF MAR as:

$$s = \frac{r}{\rho}$$

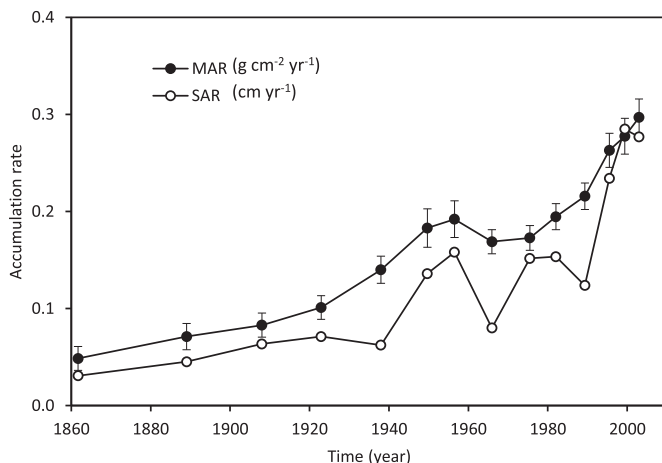following the code in Table 2 (lines 99–102) and yielding values ranging from 0.28 ± 0.02 to 0.033 ± 0.009 cm a^{-1} in the top and bottom sections, respectively (Fig. 4). The uncertainty improvement using this scheme ranged from 6 to 692%, thus making SAR also a much more meaningful magnitude. The uncertainties of MAR and SAR, even in the bottom sections, were comparable to those of other commonly measured environmental parameters. In the case of SAR, the scientist should be careful to reduce as much as possible the uncertainty of the cutting procedure. For example, when the cutting uncertainty was doubled (i.e. 0.2 mm per layer) the mean SAR uncertainty increased by 50%. This increase was not uniform as it ranged from 69% in the section 1–2 cm to 13% in the last (13–14 cm) section.

An important application of MAR is the calculation of contaminant fluxes (e.g. Ruiz-Fernández et al., 2004; Palanques et al., 2008; Diaz-Asencio et al., 2009). As an example, we included Hg concentrations (C_1, Conc1) in the dating worksheet of TEHUA II. The scheme can be easily extended to any substance concentration measured in the sedimentary record. Mercury was measured by cold-vapor atomic absorption spectrometry with an estimated mean uncertainty of 2%. Mercury concentrations ranged from 3.57 ± 0.07 in the bottom section to 53.4 ± 1.1 ng g^{-1}. The sedimentary flux of the contaminant (F_1, Flux1; (Table 2, lines 103–109) was simply calculated as:

$$F_1 = C_1 r$$

and MCU calculation followed. Mercury flux uncertainties ranged from 6.6% in the top section to 26% in the bottom section. Mercury fluxes (Fig. 5) showed a pronounced increase from layer 4 cm, corresponding to 1985.3 ± 0.7. A large number of industrial activities, including both oil refinery and cement production started in the 1970s, and large expansions were observed in the 1980s (Ruiz-Fernández et al., 2009). Indeed, both industrial activities are considered to be important sources of Hg to the environment (Pacyna et al., 2010).

We show in Fig. 6 a convergence plot of the calculation of the SAR MCU, the latest stage of ^{210}Pb radiochronology, by using the CF model for section 7–8 cm, with a convergence value of 0.016 cm a^{-1}. This value stabilized after about 4000 iterations and 10,000 iterations needed only about 5 s of computing time.

4. Dating of C1

As a rather different example of ^{210}Pb dating with MCU calculation, we chose a lacustrine sediment core with a high

Fig. 4. MAR and SAR in core TEHUA II (Gulf of Tehuantepec, Mexico). For better display, SAR uncertainty bars are not shown.
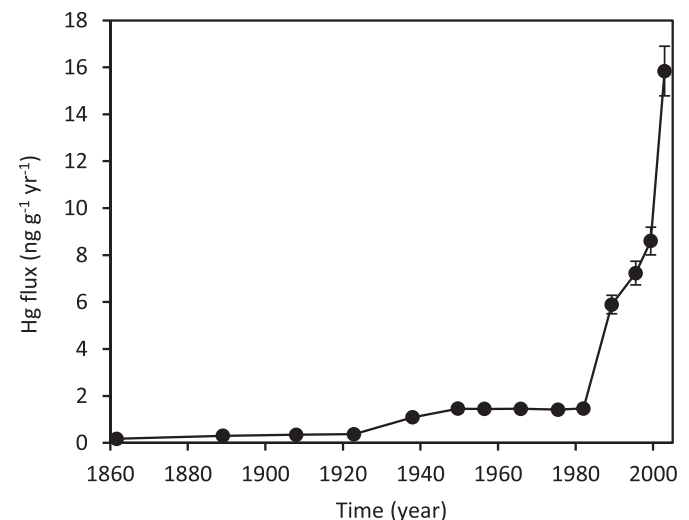

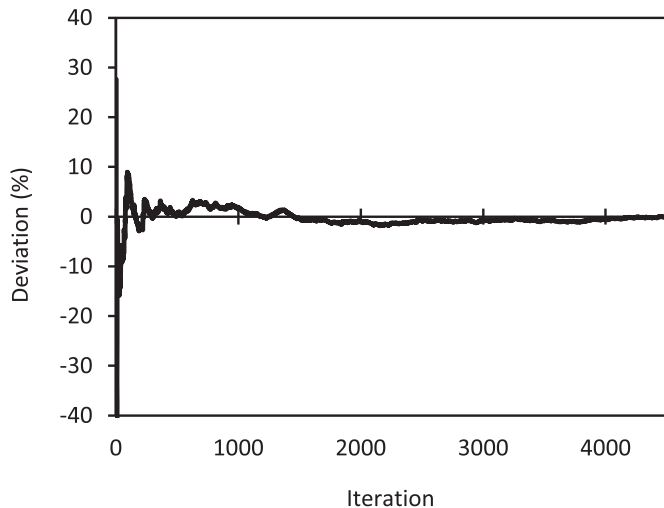Fig. 5. Mercury fluxes in core TEHUA II (Gulf of Tehuantepec, Mexico).

Fig. 6. MCU convergence (percent deviation) of SAR in core TEHUA II (section 7–8 cm).
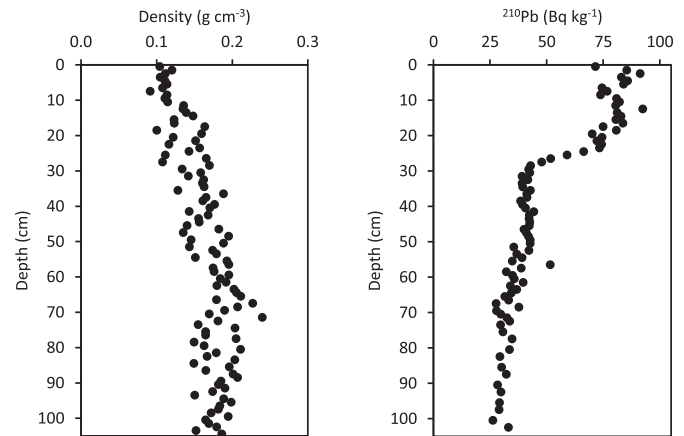

Fig. 7. Sediment bulk density (left) and ^{210}Pb activity (right) profiles of core C1 (Chapala Lake, Mexico).

accumulation rate. Chapala Lake (Jalisco State, Mexico, 1524 masl), the largest Mexican freshwater reservoir, is within the most densely developed river basin of Mexico, a major human and agricultural water supply and an important touristic attraction. The main objective of the research was to reconstruct lake environmental conditions since the beginning of the XXth century. Sediment core C1 was collected on August 2010, from location N 20° 14′ 39.3″ − W 103° 15′ 50.8″, by using a gravity (UWITEC) corer. The corer inner diameter was 8.5 ± 0.1 cm and the total core length sampled was 108 cm.

Immediately after sampling, the core was sliced into 1 cm sections, lyophilized and analyzed for ^{210}Pb by α spectrometry (through ^{210}Pb in equilibrium). A full core description and analytical methodologies can be found in Ontiveros-Cuadras et al., (2014). In order to validate the ^{210}Pb chronology, the weapons fallout tracer ^{239,240}Pu was analyzed in a nearby core (C2), which shows an identical magnetic susceptibility signal, notably a peak in the 69–70 cm section (Ontiveros-Cuadras et al., 2014). ^{239,240}Pu was purified by using ion interchange resins and electroplating (Wong, 1971; Puphal and Olsen, 1972; Merino et al., 2000). Analytical quality was achieved through the analysis of Certified Reference Materials IAEA-300 (Ballestra et al., 1994), IAEA-384 (Povinec et al., 2007) and IAEA-385 (Pham et al., 2008).

Section total masses ranged from 5.204 to 13.618 g (all measured to 0.001 g). Depth and mass related variables and uncertainties were calculated by using the MCU methodology described for core TEHUA II. Sediment bulk densities were about one order of magnitude higher than in the case of core TEHUA II and showed compaction down to about 60 cm depth (Fig. 7).

^{210}Pb activities ranged from 26.3 ± 1.7 (section 100–101 cm) to 92 ± 6 (section 12–13 cm) Bq kg^{-1}. Excess ^{210}Pb was observed down to 64 cm, thus indicating a rather high accumulation rate. We analyzed all samples of this core, but sometimes radiochronologists analyze only selected samples. Although we do not recommend this procedure, missing activities can be estimated by logarithmic interpolation of nearby sections (ln ^{210}Pb$_{ex}$ vs. accumulated mass) or by using fitting routines (e.g. Higuera et al., 2009).

The core showed 3 well defined segments: 0–24 cm (segment A), 24–29 cm (segment B) and below 29 cm (segment C). Although one might consider that segment A showed evidence of mixing, some geochemical parameters (e.g. magnetic susceptibility) revealed that the core was not mixed and, therefore, the changes observed in this segment should be attributed to changes in accumulation rates, well justified by the increasing human pressure

on the lake and the catchment basin (Ontiveros-Cuadras et al., 2014).

Following the method described by Binford (1990) we found that excess ^{210}Pb was detected down to section 63–64 cm and ^{226}Ra (supported or base ^{210}Pb) was determined as the mean of the lower subsequent sections as 31 ± 3 Bq kg^{-1}. Several sections showed low concentrations and high uncertainties, thus compromising MCU calculations if *uncertainty reduction* was not used.

The CF model with MCU was used by performing 30,000 iterations, which required about 90 s of computing time. The estimated ^{210}Pb flux was 66 ± 2 Bq m^{-2} a^{-1}, within the range of values reported by Fernex et al., (2001) in Chapala Lake and not dissimilar to ^{210}Pb$_{ex}$ sediment fluxes in other Mexican areas (Ruiz-Fernández et al., 2009). CF ages (Table 4) reached up to 167 ± 21 a, showing a maximum uncertainty improvement respect a simple QPU of up to 429%. However, it should be noted that the age uncertainty below 61 cm is over 10% and older dates should be treated with caution.

The ^{239,240}Pu profile of core C2 (Fig. 8) clearly showed two distinct features. The maximum observed in section 30–31 cm (age 1964–1965) is clearly related to the maximum weapons fallout observed in the northern troposphere in 1963 (UNSCEAR, 2000). The first detection of plutonium occurred in section 40–41 cm (age 1952–1953), also in excellent agreement with the onset of global weapons fallout (UNSCEAR, 2000).

The temporal record of core C1 showed some remarkable characteristics. Excluding sections older than 100 a (57 cm depth), sections represent in average 1.7 ± 0.8 a and, in many cases, the section time span is below or close to 1 a. This suggests that this particular sedimentary record may provide an excellent temporal resolution of interannual ecosystem changes, such as those caused by multi-annual climatic processes such as El Niño phenomenon, with periodicities of about 5 a (e.g. Moy et al., 2002).

Mass (MAR) and sediment (SAR) accumulation rates (Fig. 9), showed a similar behavior. During the last 100 a, the mean MAR uncertainty was below 30%. Though relatively large, mainly caused by the small age interval represented by sections, this value is very useful to interpret the evolution of lake sedimentation in relation with catchment activities. Since the early twentieth century accumulation rates showed a progressive increase (note: peak values in the 1910s and 1920s are affected by large uncertainties) until 1950. This trend was attributed to the overall progressive urban, agricultural and industrial development of the region. From 1952 to

Table 4
Summary of ^{210}Pb dating results of core C1 (Chapala lake, Mexico).

Code	^{210}Pb (Bq kg^{-1})	$u(^{210}$Pb)	$t(i)$ (a)	$u(t(i))$	Mean age (A.D.)	Δt_i (a)	r_i (g cm^{-2} a^{-1})	$u(r_i)$	s_i (cm a^{-1})	$u(s_i)$
C1 0–1	72	5	0.6	0.1	2010	0.6	0.162	0.022	1.55	0.22
C1 1–2	85	6	1.7	0.2	2009	1.0	0.117	0.014	0.97	0.14
C1 2–3	91	6	2.8	0.2	2008	1.1	0.102	0.011	0.92	0.13
C1 3–4	83	5	3.7	0.2	2007	0.9	0.115	0.014	1.09	0.16
C1 4–5	86	6	4.7	0.3	2006	1.1	0.106	0.012	0.95	0.14
C1 5–6	84	6	5.8	0.3	2005	1.1	0.106	0.013	0.93	0.14
C1 6–7	75	5	6.7	0.3	2004	0.9	0.125	0.017	1.16	0.18
C1 7–8	77	5	7.5	0.4	2004	0.8	0.116	0.015	1.26	0.19
C1 8–9	74	5	8.4	0.4	2003	0.9	0.121	0.016	1.06	0.16
C1 9–10	81	5	9.5	0.4	2002	1.1	0.100	0.012	0.90	0.13
C1 10–11	82	6	10.7	0.5	2000	1.2	0.094	0.012	0.82	0.12
C1 11–12	81	6	12.2	0.5	1999	1.5	0.094	0.012	0.69	0.10
C1 12–13	92	6	14.1	0.6	1997	1.9	0.072	0.008	0.53	0.07
C1 13–14	81	5	15.8	0.6	1996	1.7	0.083	0.010	0.59	0.09
C1 14–15	83	6	17.7	0.7	1994	2.0	0.076	0.009	0.51	0.07
C1 15–16	81	6	19.4	0.7	1992	1.6	0.075	0.010	0.61	0.09
C1 16–17	84	6	21.2	0.8	1990	1.9	0.067	0.008	0.54	0.08
C1 17–18	75	5	23.4	0.9	1988	2.2	0.075	0.010	0.46	0.07
C1 18–19	81	5	25.0	0.9	1986	1.6	0.063	0.008	0.62	0.09
C1 19–20	70	5	27.1	1.0	1985	2.1	0.075	0.011	0.47	0.08
C1 20–21	75	5	29.1	1.1	1982	1.9	0.063	0.008	0.52	0.08
C1 21–22	72	5	31.5	1.2	1980	2.4	0.063	0.008	0.41	0.06
C1 22–23	74	5	33.6	1.3	1978	2.1	0.055	0.008	0.48	0.08
C1 23–24	73	5	36.6	1.4	1975	3.0	0.052	0.007	0.33	0.05
C1 24–25	66	4	39.1	1.5	1973	2.5	0.058	0.009	0.40	0.07
C1 25–26	59	4	40.7	1.6	1971	1.6	0.068	0.012	0.61	0.12
C1 26–27	52	3	42.6	1.7	1969	1.9	0.087	0.019	0.52	0.12
C1 27–28	48	3	43.7	1.8	1967	1.1	0.103	0.026	0.95	0.25
C1 28–29	43	3	44.9	1.9	1966	1.2	0.140	0.046	0.82	0.28
C1 29–30	42	3	45.8	1.9	1965	0.9	0.146	0.051	1.09	0.39
C1 30–31	43	3	47	2	1964	1.2	0.136	0.048	0.86	0.31
C1 31–32	39	3	48	2	1963	0.8	0.186	0.084	1.31	0.60
C1 32–33	42	3	49	2	1962	1.2	0.138	0.049	0.85	0.31
C1 33–34	39	2	50	2	1961	0.9	0.175	0.078	1.09	0.49
C1 34–35	40	2	51	2	1960	1.0	0.164	0.070	1.01	0.44
C1 35–36	43	3	52	2	1959	1.1	0.113	0.038	0.88	0.30
C1 36–37	41	3	53	2	1958	1.5	0.126	0.046	0.67	0.25
C1 37–38	41	3	55	2	1956	1.4	0.119	0.043	0.72	0.27
C1 38–39	39	2	56	2	1955	1.0	0.158	0.077	0.98	0.49
C1 39–40	39	3	57	3	1954	1.3	0.137	0.063	0.77	0.36
C1 40–41	41	3	59	3	1953	1.5	0.113	0.045	0.66	0.27
C1 41–42	44	3	61	3	1951	1.8	0.078	0.024	0.54	0.17
C1 42–43	42	3	63	3	1949	2.0	0.086	0.030	0.51	0.18
C1 43–44	42	3	64	3	1947	1.9	0.082	0.029	0.52	0.19
C1 44–45	43	3	67	3	1945	2.1	0.075	0.026	0.48	0.17
C1 45–46	42	3	69	3	1943	2.0	0.071	0.025	0.51	0.18
C1 46–47	40	3	71	3	1941	2.2	0.084	0.036	0.46	0.20
C1 47–48	41	3	73	4	1939	1.9	0.071	0.028	0.52	0.21
C1 48–49	42	3	76	4	1936	3.3	0.060	0.022	0.31	0.11
C1 49–50	43	3	79	4	1933	2.9	0.051	0.018	0.35	0.12
C1 50–51	43	3	83	5	1930	4.1	0.046	0.015	0.24	0.08
C1 51–52	36	2	84	5	1927	1.3	0.112	0.091	0.78	0.64
C1 52–53	42	3	88	5	1924	4.3	0.040	0.015	0.23	0.09
C1 53–54	37	3	91	5	1921	2.5	0.071	0.045	0.39	0.25
C1 54–55	39	3	94	6	1918	3.3	0.046	0.022	0.30	0.14
C1 55–56	35	2	96	6	1915	2.1	0.090	0.084	0.47	0.44
C1 56–57	52	4	112	9	1906	15.5	0.013	0.003	0.07	0.02
C1 57–58	39	3	120	11	1895	7.5	0.023	0.012	0.13	0.07
C1 58–59	32	2	121	10	1890	1.2	0.144	0.453	0.82	2.58
C1 59–60	35	2	126	11	1887	5.4	0.037	0.033	0.19	0.17
C1 60–61	36	3	133	12	1881	7.3	0.025	0.020	0.14	0.11
C1 61–62	40	3	155	19	1866	21.9	0.009	0.005	0.05	0.02
C1 62–63	34	3	167	21	1849	11.9	0.015	0.018	0.09	0.10

1965 (upper end of segment C) accumulation rates abruptly increased, reaching a maximum in 1963. This period is coincident with a series of droughts in the area and led to minimum lake levels in 1955 and 1958 (CONAGUA, 2013). A less pronounced but similar behavior was observed since 1998 to 2004, which was also related to low lake levels due to droughts and lake water management in 2001 and 2002 (SEMARNAT, 2006). We suggest that increased sedimentation in these periods may be related to erosion and transport of emerged lake margin sediments, and possible eutrophication of lake waters. Since 1966 to 1974 (segment B) the lake returned to a low sedimentation regime due to the increase of water levels. Since then (segment A), the progressive increase in accumulation rates observed before 1952 continued, until reaching a recent maximum at the core surface.
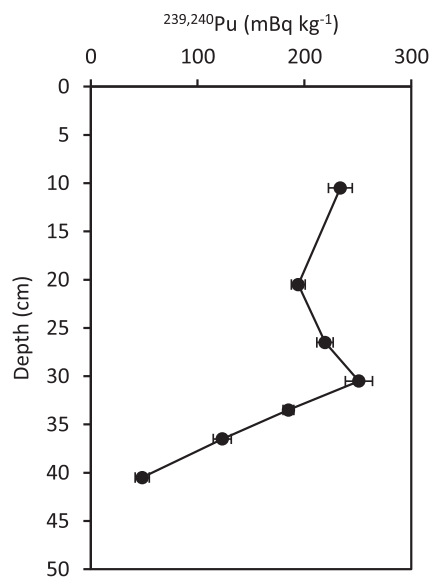
Fig. 8. ^{239,240}Pu concentration in core C2 (Chapala Lake, Mexico).

5. Dating of CHL1

As a final application example, we dated a bog core. As ombrotrophic bog mires receive nutrients only from the atmosphere, it is expected a minimum input of lithogenic substances such as ^{226}Ra. The peat core CHL1 was collected from the Chao de Lamoso mire (43.50°N 7.56°W), a blanket bog in Sierra do Xistral (Galicia, Spain) and it is fully described in a series of papers aimed to provide Southern Europe records of atmospheric contaminant fluxes (Olid et al., 2008, 2010 and 2013).

The peat bog core was collected using a Wardenaar sampler (100 cm^2 surface), immediately sampled into 1 cm (above 8 cm) and 2 cm (below 8 cm) sections. Surface vegetation was also sampled and, in this work, considered as the first 1 cm section. ^{210}Pb in dry samples was determined by α spectrometry through ^{210}Pb in equilibrium, following a method described by Sanchez-Cabeza et al., (1998). ^{226}Ra was measured by γ spectrometry with a high-purity intrinsic Ge detector but it was below the detection limit (*circa* 5.5 Bq kg^{-1}), in agreement with the ombrotrophic nature of the bog and its low mineral contents (Olid et al., 2008).

The core was 30 cm long and densities ranged from 0.091 (top) to 0.132 (bottom) g cm^{-3}. Total ^{210}Pb activities, assumed to be equal

to ^{210}Pb$_{ex}$, ranged from 472 ± 19 Bq kg^{-1} in the first core section to 4.8 ± 1.2 Bq kg^{-1} in the bottom section. The bottom core layer age was 187 ± 8 a (4% uncertainty), thus showing an uncertainty below 10% beyond 150 a (Table 5). Excluding the surface vegetation, the time resolution ranged from 4 a in section 6–7 cm to 38 a in the bottom section, with a mean value of 12 a. It was concluded that this core could provide valuable information on the decadal changes of atmospheric pollution fluxes in the region (Olid et al., 2013). In all cases, age MCU were sensibly smaller than QPU: excluding the top layer (where it was 5 times smaller), MCU reduction ranged from 27% (section 4–5 cm) to 42% (section 1–3 cm), with a mean uncertainty reduction of 34%.

Bog accretion (Fig. 10) increased from 0.0189 ± 0.0007 g cm^{-2} a^{-1} in the top section to an almost constant value in segment 5–22 cm (mean 0.0225 ± 0.0011 g cm^{-2} a^{-1}) and decreased to 0.0073 ± 0.0010 g cm^{-2} a^{-1} in the bottom section (28–30 cm). MAR QPU ranged from 4% to 14% in the top and bottom sections, respectively. This allows the rather precise determination of contamination fluxes in this record (Olid et al., 2013).

6. Discussion

6.1. MAR uncertainties

The ^{210}Pb dating uncertainty sources considered in this work were i) core diameter, ii) ^{210}Pb half-life, iii) depth of core cutting, iv) section dry mass, v) ^{210}Pb total concentration and vi) ^{226}Ra concentration (except in the peat bog core CHL1). These magnitudes were simulated for 3 cores by using a simple Monte Carlo methodology assuming Gaussian distributions, and the uncertainties were estimated from 30,000 simulations.

Since 1900, MAR uncertainties of core TEHUA II were rather constant and values ranged from 0.012 to 0.020 g cm^{-2} a^{-1}. The mean MAR relative uncertainty was 9%, thus providing excellent conditions for the derivation of other mass related quantities such as cyst fluxes (Sanchez-Cabeza et al., 2012). In the case of core C1, MAR uncertainties remained below 0.02 g cm^{-2} a^{-1} since 1969 to present, with a mean MAR relative uncertainty of 13%. During the peak sedimentation period in the 50s and 60s, uncertainties were as high as 0.084 g cm^{-2} a^{-1} and the mean relative value was 38%. From 1930 to 1951, MAR uncertainties ranged from 0.015 to 0.036 g cm^{-2} a^{-1}, with a mean value of 36%. Below this segment, because of the low ^{210}Pb$_{ex}$ activities observed, MAR uncertainties
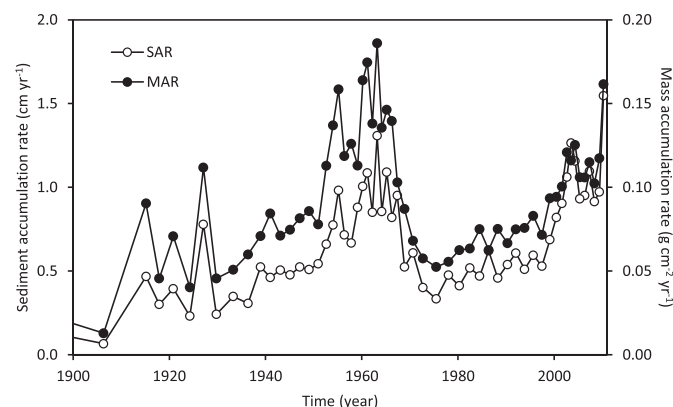

Fig. 9. SAR and MAR in core C1 (Chapala lake, Mexico). Uncertainties can be found in the Supplementary information.

Table 5
CF (Constant Flux) ages and Monte Carlo derived uncertainties in core CHL 1 (Chao de Lamoso, NW Spain).

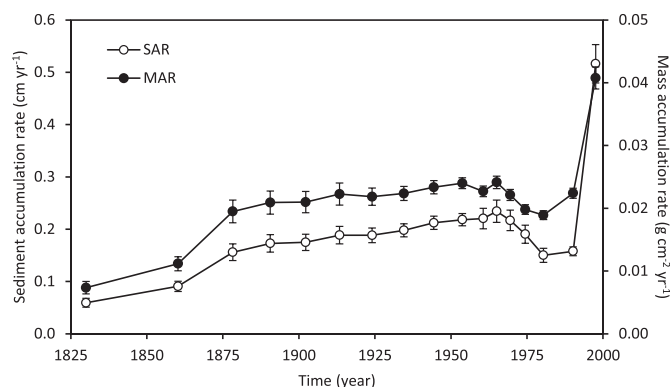| Layer (cm)	CF age (a)	Calendar age (A.D.)	Age uncertainty (a)	Section (cm)	Mean calendar age (a)
0.0	0.0	1998.5	0.0	0–1	1997.6
1.0	1.9	1996.6	0.1	1–3	1990.2
3.0	14.8	1983.7	0.4	3–4	1980.4
4.0	21.5	1977.1	0.5	4–5	1974.4
5.0	26.7	1971.8	0.5	5–6	1969.5
6.0	31.4	1967.2	0.6	6–7	1965.0
7.0	35.6	1962.9	0.6	7–8	1960.6
8.0	40.2	1958.4	0.7	8–10	1953.7
10.0	49.4	1949.1	0.8	10–12	1944.4
12.0	58.9	1939.6	0.9	12–14	1934.5
14.0	69.1	1929.4	1.1	14–16	1924.1
16.0	79.8	1918.7	1.3	16–18	1913.4
18.0	90.5	1908.0	1.4	18–20	1902.2
20.0	102.1	1896.4	1.7	20–22	1890.6
22.0	114	1885	2	22–24	1878
24.0	127	1872	3	24–26	1860
26.0	150	1849	4	26–28	1830
28.0	187	1811	8		

Fig. 10. SAR and MAR in core CHL 1 (Chao de Lamoso, NW Spain).

become erratic, with a mean deviation of 88% and should not be used to derive other parameters or discuss accumulation rates. MAR uncertainties in core CHL1 where the lowest in this work, mostly due to the fact that ^{226}Ra was not considered as an uncertainty source. MAR uncertainty values ranged from 0.0008 g cm^{-2} a^{-1} (4%) in the surface section to 0.001 g cm^{-2} a^{-1} (14%) in the bottom section. The mean MAR uncertainty in core CHL1 was 6%, thus confirming its suitability as environmental record.

6.2. Uncertainty budgets

Accumulation rate uncertainties in all cores suggest that the uncertainty sources are quite different for the simulated magnitudes. In Table 6 we show the detailed uncertainty budget calculation for the CF layer age, MAR and SAR in core TEHUA II. The smallest relative uncertainty corresponded to the section mass (<0.001%) and, consequently, its contribution to the uncertainty budget was always less than 1%. The ^{210}Pb decay constant (λ) had a mean 2% contribution to the CF layer age ($t(i)$) and a close to zero contribution to the accumulation rates. It is not surprising that the inner core diameter measurement did not affect the CF layer age, as the dating equations used in this work do not contain the core surface area, but can have an up to 3% contribution to MAR.

The largest overall contribution to all radiochronologically derived variables were, not unexpectedly, the radionuclide concentrations. The ^{210}Pb uncertainty contribution to the CF layer age was largest in the top sections and decreased with depth as it approached the base value and, complementary, the ^{226}Ra uncertainty contribution increased until reaching a similar contribution to ^{210}Pb in the core bottom. A similar result was observed for the calculation of MAR. For the CF layer age and MAR, the added uncertainty contributions from both radionuclides were always >95%. If these were the only variables of interest, a special effort should be done to reduce the concentration uncertainties, but the discussion of this is out of the scope of this work.

A different picture emerged when SAR budget uncertainties were examined. In average, about 43% of the uncertainty budget was due to the section thicknesses, and this was up to 63% in section TEH II 3–4. The remaining 57% is mostly shared amongst the radionuclide activities.

A similar result was obtained for core C1 (data not shown). The largest mean contributions to the CF layer age uncertainty were due to ^{210}Pb (59%) and ^{226}Ra (40%) concentrations, and only 1% due to the decay constant. In the case of MAR, the mean uncertainty contributions of the ^{210}Pb and ^{226}Ra concentrations, and λ were 62%, 37% and 1%, respectively. In the case of SAR, the uncertainty contribution from depth was 14% (with a maximum value of 35% in

section C1 2–3), and mean values of 52% and 33% for ^{210}Pb and ^{226}Ra, respectively.

As ^{226}Ra concentrations were assumed to be zero in core CHL1, somewhat different results were obtained in this case. As expected, the single largest contribution to the CF layer age uncertainty was the ^{210}Pb concentration (mean 91%), but in this case the decay constant contributed with a mean 8% (maximum 12%), its largest contribution in this work. This emphasizes the need to systematically consider all uncertainty sources in ^{210}Pb dating. In the case of MAR, the ^{210}Pb contribution (93%) was followed by the layer depth (6%). In contrast, the layer depth had a particularly large contribution in SAR uncertainty (48%), of the same order of magnitude than ^{210}Pb (52%).

These results confirm that special attention must be paid by radiochronologists to reduce as much as possible the measurement uncertainties of the radionuclides and that, in the case that SAR is a relevant magnitude, special care is needed to reduce as much as

Table 6
Uncertainty budget for CF ^{210}Pb dating of core TEHUA II (Gulf of Tehuantepec).

Code	Relative uncertainty (%)					
	ϕ	λ	$z(i)$	Δm_i	^{210}Pb	^{226}Ra
TEH 7–8	0.58	0.54	0.72	0.00061	5.9	8.6
u(t(i)) uncertainty fraction (%)						
TEH 0–1	0	1	0	0	93	6
TEH 1–2	0	1	0	0	91	7
TEH 2–3	0	2	0	0	90	8
TEH 3–4	0	2	0	0	87	11
TEH 4–5	0	3	0	0	84	13
TEH 5–6	0	3	0	0	81	16
TEH 6–7	0	3	0	0	76	21
TEH 7–8	0	3	0	0	74	23
TEH 8–9	0	3	0	0	72	25
TEH 9–10	0	3	0	0	65	32
TEH 10–11	0	2	0	0	61	37
TEH 11–12	0	2	0	0	58	40
TEH 12–13	0	1	0	0	54	45
TEH 12–14	0	0	0	0	52	48
Mean	*0*	*2*	*0*	*0*	*74*	*24*
u(r_i) uncertainty fraction (%)						
TEH 0–1	3	1	0	0	90	6
TEH 1–2	3	1	0	0	90	6
TEH 2–3	3	1	0	0	89	7
TEH 3–4	3	1	0	0	88	8
TEH 4–5	3	1	0	0	87	9
TEH 5–6	2	1	0	0	87	10
TEH 6–7	2	1	0	0	82	15
TEH 7–8	1	0	0	0	79	20
TEH 8–9	1	0	0	0	77	21
TEH 9–10	1	0	0	0	73	26
TEH 10–11	1	0	0	0	69	30
TEH 11–12	1	0	0	0	64	36
TEH 12–13	0	0	0	0	58	42
TEH 12–14	0	0	0	0	53	47
Mean	*2*	*0*	*0*	*0*	*78*	*20*
u(s_i) uncertainty fraction (%)						
TEH 0–1	0	0	46	0	51	3
TEH 1–2	0	0	62	0	36	2
TEH 2–3	0	0	61	0	36	3
TEH 3–4	0	0	63	0	34	3
TEH 4–5	0	0	59	0	37	4
TEH 5–6	0	0	55	0	40	5
TEH 6–7	0	0	56	0	37	7
TEH 7–8	0	0	41	0	47	12
TEH 8–9	0	0	37	0	50	14
TEH 9–10	0	0	41	0	44	15
TEH 10–11	0	0	32	0	47	21
TEH 11–12	0	0	23	0	49	28
TEH 12–13	0	0	16	0	49	35
TEH 12–14	0	0	9	0	48	43
Mean	*0*	*0*	*43*	*0*	*43*	*14*

possible the uncertainty during core sectioning. However, we recognize that improving the cutting precision, especially in field conditions, may be a difficult task and further work needs to be done in this respect.

6.3. Method summary

The radiochronologist must carefully assess which uncertainty sources are relevant in each experiment. In this method we consider 6 uncertainty sources: core diameter (or square length), ^{210}Pb half-life, layer depth, section dry mass, and ^{210}Pb total and ^{226}Ra concentrations. Data are properly organized in an Excel workbook, in which iteration calculation (number of iterations = 1) is allowed and Switch and Counter cells are defined. Measured magnitudes are simulated using a Monte Carlo (randomized) approach. Derived variables are calculated using the random values obtained for each iteration, the accumulated quadratic deviation from the true value is calculated and, finally, the uncertainty is obtained. In order to avoid calculation errors due to random values close to zero, we propose an *uncertainty reduction* scheme by which measured uncertainties are dived by a constant factor, which is later multiplied to the resulting uncertainties.

The MCU strategy described, though apparently more complex than QPU for simple expressions, is very robust as i) uncertainties are calculated always with the same simple principles and ii) it does not require the derivation and use of complex formulae, thus reducing the probability of errors. The accompanying Excel wokbooks (Supplementary Information) can be easily adapted for each researcher needs. Once all needed values and expressions have been entered, Switch must be set to zero in order to delete all square sum calculations. Then, from the blank sheet (in order to reduce computing time) the desired number of iterations can be selected from the *File − Options − Formulas* menu. Although the number of iterations used in this work was 30,000, the number could be reduced to about 10,000 without loss of precision. Before taking any other action, the number of iterations is again set to 1 (or disabled if no more calculations are to be performed).

7. Conclusions

In this work, we describe a simple method for the calculation of ^{210}Pb dating uncertainties using a Monte Carlo method, implemented in a commonly-used proprietary spreadsheet software. We believe that the simple scheme proposed can be useful because i) nowadays, computers performance allows long calculations in short times, ii) there is no need to develop long and cumbersome equations based on the quadratic propagation law, iii) the uncertainty calculation scheme is simple an repetitive, and iv) it helps to define the main uncertainty sources.

We successfully used the proposed MCU scheme to compute uncertainties of radiochronologically-derived parameters in three contrasting cores: marine and lake sediments, and a peat bog. The maximum computing time required for 30,000 iterations was about 90 s. Monte Carlo uncertainties were always lower than uncertainties derived by simple quadratic propagation, or when quadratic propagation included dependent variables. The MCU analysis confirmed the relevance of the ^{210}Pb and ^{226}Ra concentrations as the main uncertainty contributors to ages and MAR. In case of SAR, the precision of core cutting becomes a third dominant uncertainty source. The use of the described method goes beyond ^{210}Pb dating and could be used in any field of the analytical sciences, including other radiochronological applications.

Appendix A. Supplementary data

Supplementary data related to this article can be found at http://dx.doi.org/10.1016/j.quageo.2014.06.002.

References

Appleby, P.G., Oldfield, F., 1978. The calculation of ^{210}Pb dates assuming a constant rate of supply of unsupported ^{210}Pb to the sediment. Catena 5, 1–8.

Appleby, P.G., 2001. Chronostratigraphic techniques in recent sediments. In: Last, W.M., Smol, J.P. (Eds.), Tracking Environmental Change Using Lake Sediments, Basin Analysis, Coring and Chronological Techniques, vol. 1. Kluwer Academic Publishers, Dordrecht, The Netherlands, pp. 171–201.

Ballestra, S., Gastaud, J., Lopez, J.J., Parsi, P., Vas, D., 1994. Report on the Intercomparison Run IAEA-300: Radionuclides in Marine Sediment. IAEA/AL/064. IAEA, Monaco.

Binford, M.W., 1990. Calculation and uncertainty analysis of 21 dates for PIRLA project lake cores. J. Paleolimnol. 3, 253–268.

CONAGUA (Comisión Nacional del Agua), 2013. Niveles máximos y mínimos del Lago Chapala 1900-2013 consulted from: http://www.ceajalisco.gob.mx/sia/niveles/niveles.html. on 11/07/2013 (last updated 13/06/2013).

DDEP − DATA DECAY EVALUATION PROJECT, 2012. LNE-LNHB/CEA − Table de radionucléides ^{210}Pb consulted from: http://www.nucleide.org/DDEP_WG/DDEPdata.htm. updated 6/1/2012.

Diaz-Asencio, M., Alonso-Hernandez, C., Bolaños-Alvarez, Y., Gomez-Batista, M., Pinto, V., Morabito, R., Hernandez-Albernas, J., Eriksson, M., Sanchez-Cabeza, J.A., 2009. One century sedimentary record of Hg and Pb pollution in the Sagua estuary (Cuba) derived from ^{210}Pb and ^{137}Cs chronology. Mar. Pollut. Bull. 59, 108–115.

Ellison, S.L.R., Mosslein, M., Williams, A., 2000. Guide Quantifying Uncertainty in Analytical Measurement, second ed. EURACHEM/CITAC, London.

Fernex, F., Zárate-del Valle, P., Ramírez-Sánchez, H., Michaud, F., Parron, C., Dalmasso, J., Barci-Funel, G., Guzman-Arroyo, M., 2001. Sedimentation rates in Lake Chapala (western Mexico): possible active tectonic control. Chem. Geol. 177 (3–4), 213–228.

Hellstrom, J., 2006. U−Th dating of speleothems with high initial ^{230}Th using stratigraphical constraint. Quat. Geochronol. 1 (4), 289–295.

Higuera, P.E., Brubaker, L.B., Anderson, P.M., Hu, F.S., Brown, T.A., 2009. Vegetation mediated the impacts of postglacial climate change on fire regimes in the south-central Brooks Range, Alaska. Ecol. Monogr. 79, 201–219.

IPCC, 2007. In: Core Writing Team, Pachauri, R.K., Reisinger, A. (Eds.), Climate Change 2007: Synthesis Report. Contribution of Working Groups I, II and III to the Fourth Assessment Report of the Intergovernmental Panel on Climate Change. IPCC, Geneva, Switzerland.

ISO, 1995. Guide to Expression of Uncertainty in Measurement. International Organization for Standardisation, Geneva, Switzerland.

Krishnaswamy, S., Lal, D., Martin, J., Meybeck, M., 1971. Geochronology of lake sediments. Earth Planet. Sci. Lett. 11, 407–414.

Lynch, J.C., Meriwether, J.R., McKee, B.A., Vera-Herrera, F., Twilley, R.R., 1989. Recent accretion in mangrove ecosystems based on ^{137}Cs and ^{210}Pb. Estuar. Coast. 12 (4), 284–299.

Merino, J., Sanchez-Cabeza, J.A., Pujol, Ll, Leonard, K., McCubbin, D., 2000. Plutonium activity ratios in plankton: new evidence of hold-up time in Irish Sea sediments. J. Radioanal. Nucl. Chem. 243, 517–524.

Moy, C., Seltzer, G.O., Rodbell, D.T., Anderson, D.M., 2002. Variability of El Niño/Southern oscillation activity at millennial timescales during the Holocene epoch. Nature 420, 162–165.

Olid, C., Garcia-Orellana, J., Martinez-Cortizas, A., Masque, P., Peiteado, E., Sanchez-Cabeza, J.A., 2008. Role of surface vegetation in ^{210}Pb-dating of peat cores. Environ. Sci. Technol. 42 (23), 8858–8864.

Olid, C., Garcia-Orellana, J., Martínez Cortizas, A., Masqué, P., Peiteado-Varela, E., Sanchez-Cabeza, J.A., 2010. Multiple site study of atmospheric metal (Pb, Zn and

Cu) deposition in the NW Iberian Peninsula using peat cores. Sci. Total Environ. 408, 5540–5549.

Olid, C., Garcia-Orellana, J., Masqué, P., Martínez Cortizas, A., Sanchez-Cabeza, J.A., Bindler, R., 2013. Improved ^{210}Pb-chronology of Pb deposition in three peat cores from Chao de Lamoso (NW Spain). Sci. Total Environ. 443, 597–607.

Ontiveros-Cuadras, J.F., Ruiz-Fernández, A.C., Sanchez-Cabeza, J.A., Pérez-Bernal, L.H., Sericano, J.L., Preda, M., Liong Wee Kwong, L., Páez-Osuna, F., 2014. Trace element fluxes and natural potential risks from ^{210}Pb-dated sediment cores in lacustrine environments at the Central Mexican Plateau. Sci. Total Environ. 468–469, 677–687.

Pacyna, E.G., Pacyna, J.M., Sundseth, K., Munthe, J., Kindbom, K., Wilson, S., Steenhuisen, F., Maxson, P., 2010. Global emission of mercury to the atmosphere from anthropogenic sources in 2005 and projections to 2020. Atmos. Environ. 44, 2487–2499.

Palanques, A., Masqué, P., Puig, P., Sanchez-Cabeza, J.A., Frignani, M., Alvisi, F., 2008. Anthropogenic trace metals in the sedimentary record of the Llobregat continental shelf and adjacent Foix Submarine Canyon (northwestern Mediterranean). Mar. Geol. 248 (3–4), 213–227.

Pham, M.K., Sanchez-Cabeza, J.A., Povinec, P.P., Andor, K., Arnold, D., Benmansour, M., Bikit, I., Carvalho, F., Dimitrova, K., Edrev, Z.H., Engeler, C., Fouche, F.J., Garcia-Orellana, J., Gascó, C., Gastaud, J., Gudelis, A., Hancock, G., Holm, E., Legarda, F., Ikäheimonen, T.K., Ilchmann, C., Jenkinson, A.V., Kanisch, G., Kis-Benedek, G., Kleinschmidt, R., Koukouliou, V., Kuhar, B., LaRosa, J., Lee, S.-H., LePetit, G., Levy-Palomo, I., Liong Wee Kwong, L., Llauradó, M., Maringer, F.J., Meyer, M., Michalik, B., Michel, H., Nies, H., Nour, S., Oh, J.-S., Oregioni, B., Palomares, J., Pantelic, G., Pfitzner, J., Pilvio, R., Puskeiler, L., Satake, H., Schikowski, J., Vitorovic, G., Woodhead, D., Wyse, E., 2008. A new certified reference material for radionuclides in Irish sea sediment (IAEA-385). J. Appl. Radiat. Isot. 66, 1711–1717.

Povinec, P.P., Pham, M.K., Sanchez-Cabeza, J.A., Barci-Funel, G., Bojanowski, R., Boshkova, T., Burnett, W.C., Carvalho, F., Chapeyron, B., Cunha, I.L., Dahlgaard, H., Galabov, N., Gastaud, J., Geering, J.-J., Gomez, I.F., Green, N., Hamilton, T., Ibanez, F.L., Ibn Majah, M., John, M., Kanisch, G., Kenna, T.C., Kloster, M., Korun, M., Liong Wee Kwong, L., La Rosa, J., Lee, S.-H., Levy-Palomo, I., Malatova, M., Maruo, Y., Mitchell, P., Murciano, I.V., Nelson, R., Oh, J.-S., Oregioni, B., Le Petit, G., Pettersson, H.B.L., Reineking, A., Smedley, P.A., Suckow, A., van der Struijs, T.D.B., Voors, P.I., Yoshimizu, K., Wyse, E., 2007. Reference material for radionuclides in sediment, IAEA-384 (Fangataufa Lagoon sediment). J. Radioanal. Nucl. Chem. 273 (2), 383–393.

Puphal, K.W., Olsen, D.R., 1972. Electrodeposition of alpha-emitting nuclides from a mixed oxalate-chloride electrolyte. Anal. Chem. 44 (2), 284–289.

Ramsey, C.B., van der Plicht, J., Weninger, B., 2001. 'Wiggle matching' radiocarbon dates. Radiocarbon 43 (2A), 381–389.

Refsgaard, J.C., van der Sluijs, Jeroen P., Højberg, A.L., Vanrolleghem, P.A., 2007. Uncertainty in the environmental modelling process − a framework and guidance. Environ. Model. Softw. 22 (11), 1543–1556.

Robbins, J.A., 1978. Geochemical and geophysical applications of radioactive lead isotopes. In: Nriagu, J.O. (Ed.), Biochemistry of Lead. Elsevier, Amsterdam, pp. 85–393.

Ruiz-Fernández, A.C., Páez-Osuna, F., Urrutia-Fucugauchi, J., Preda, M., Rehault, I., 2004. Historical trace metal fluxes in the Mexico City Metropolitan Zone as evidenced by a sedimentary record from the Espejo de los Lirios lake. J. Environ. Monit. 6 (5), 473–480.

Ruiz-Fernández, A.C., Hillaire-Marcel, C., de Vernal, A., Machain-Castillo, M.L., Vásquez, L., Ghaleb, B., Aspiazu-Fabián, J.A., Páez-Osuna, F., 2009. Changes of coastal sedimentation in the Gulf of Tehuantepec, South Pacific Mexico, over the last 100 years from short-lived radionuclide measurements. Estuar. Coast. Shelf Sci. 82 (3), 525–536.

Sanchez-Cabeza, J.A., Masqué, P., Ani-Ragolta, I., 1998. [210]Pb and [210]Po analysis in sediments and soils by microwave acid digestion. J. Radioanal. Nucl. Chem. 227 (1–2), 19–22.

Sanchez-Cabeza, J.A., Ruiz-Fernández, A.C., 2012. [210]Pb sediment radiochronology: an integrated formulation and classification of dating models. Geochim. Cosmochim. Acta 82, 183–200.

Sanchez-Cabeza, J.A., Ruiz-Fernández, A.C., de Vernal, A., Machain-Castillo, M.L., 2012. Reconstruction of pyrodinium blooms in the tropical East Pacific (Mexico): are they related to ENSO? Environ. Sci. Technol. 46 (12), 6830–6834.

SEMARNAT (Secretaria de Medio Ambiente y Recursos Naturales), 2006. Acuerdo por el que se da a conocer el estudio técnico de los recursos hídricos del área geográfica Lerma-Chapala. SEMARNAT Diario Oficial, 8–50, 24 de Julio de 2006, (in Spanish).

Taylor, B.N., Kuyatt, C.E., 1994. Guidelines for Evaluating and Expressing the Uncertainty of NIST Measurement Results. NIST Tech. Note 1297. U.S. Government Printing Office, Washington, D.C.

UNSCEAR (United Nations Scientific Committee on the Effects of Atomic Radiation), 2000. Report to the General Assembly, with Scientific Annexes. United Nations, NewYork.

Wong, K.M., 1971. Radiochemical determination of plutonium in sea water, sediments and marine organisms. Anal. Chim. Acta 56, 355–364.